Halide Perovskite Photodiode Integrated CMOS Imager

Wenya Song[1†], Jubin Kang[1,3,5†], Karim Elkhouly[1,2], Sarah Hamdad[1,2], Xin Zhang[1,4], Isabel Pintor Monroy[1], Abu Bakar Siddik[1,2], Patrick Carolan[1], Sownder Subramaniam[1,2], Yinghuan Kuang[1], Florian De Roose[1], Erwin Vandenplas[1], Naresh Chandrasekaran[1], Joo Hyoung Kim[1], Robert Gehlhaar[1], Seong-Jin Kim[5], Jiwon Lee[1,6,] and Jan Genoe[1,2,*]*

[1]imec, Leuven, 3001, Belgium

[2]ESAT, KU Leuven, 3001 Heverlee, Belgium

[3]Ulsan National Institute of Science and Technology, Ulsan, Korea

[4] Fudan University, Shanghai, China

[5]Sogang University, Seoul, Korea

[6]Pohang University of Science and Technology, Pohang, Korea

[†]These authors contributed equally

ABSTRACT

Thin film photodiodes (TFPD) can supplement complementary metal-oxide-semiconductor (CMOS) image sensor vision by their exotic optoelectronic properties assisted by their monolithic processibility. Halide perovskites are known to show outstanding optoelectronic properties such as large absorption coefficient, long carrier diffusion lengths, and high carrier mobility, leading to high external quantum efficiency (EQE) and fast charge transport in photodiodes (PDs), especially compared with other thin-film photodiode candidates. In this paper, high resolution 2-dimensional (2D) and 3-dimensional (3D) imaging capabilities are demonstrated with this novel PD material on the silicon (Si) read-out integrated circuit (ROIC). The integration of this perovskite photodiode (PePD) on Si ROIC provides fine resolution for 2D imaging. Fast carrier transport properties of PePD enable sensing the depth of the objects with the same sensor. 3D imaging is demonstrated with the proposed top-electrode controlled indirect time-of-flight (iToF) operation supported by the fast PD switching through the top common electrode of the TFPD image sensor pixel. It is expected that the PePDs on Si ROIC could open a new chapter for the TFPD imaging platform with its outstanding optoelectronic performance in combination with the CMOS image sensor technology, not just for rather conventional 2D imaging, but while enabling the extension towards the 3D sensing, promising for applications such as automotive, augmented reality (AR) and virtual reality (VR).

KEYWORDS

Halide perovskite, photodetector, photodiode, carrier transit time, CMOS ROIC, image sensor, color imaging, indirect time-of-flight

INTRODUCTION

Si is well established as a detector material for cameras in the visible wavelength, as it outperforms by far in the combination of almost all relevant performance metrics, i.e. high EQE[1] over the entire visible wavelength range, very low dark current,[2] excellent linearity and dynamic range[3,4] and last but not least very strong scalability[5] down to 0.5 µm. However, Si has an absorption length for red wavelengths (640 nm) of about 6 µm, which requires an absorption layer thickness of about the same range. The need for thicker photodiodes to implement efficient photodiodes, which generally makes classical photodiode response difficult to achieve below the microsecond level.[6] The charge collection speed in Si can be increased by either (1) increasing the electric field (e.g. single photon avalanche diode (SPAD),[7,8]) which requires additional area and hence substantially limits the pixel scaling or (2) by reducing the effective charge collection depth,[9] which comes with a substantial absorption and EQE penalty. Meanwhile, to increase the effective absorption length and avoid color crosstalk in Si, researchers developed anti-reflection, backside scattering structures and deep trench isolation technologies[10–13]. The doping profile of Si absorber has also been optimized to increase charge collection speed[14,15]. However, overcoming this trade-off between absorption efficiency and response time remains a challenge.

The charge collection speed can also be improved by introducing a new detector material on top of the Si ROIC, but in prior art, crystalline materials such as Ge and InGaAs have shown problems with pixel down scalability[16,17], and amorphous detector materials such as organic semiconductors report low mobilities[18]. Beyond standard photography, ToF based image sensors can generate a 3D image, relying on a fast-responding photodiode to capture depth information.[15,19–25] Halide perovskites are a class of materials with unique optical and electrical properties, such as large extinction coefficients,[26,27] long carrier diffusion lengths,[28–30] and high carrier mobilities.[31] These

attributes enable efficient broadband light absorption and fast charge transport, leading to EQE close to unity applicable in high-speed photodiodes (PD).[32] Naturally, integrating thin film PePD on CMOS ROIC will enable applications such as the combination of 3D sensing based on ToF with high-resolution, high efficiency 2D imaging.

There have been various attempts to implement high-resolution PePD image sensors to leverage optical and electrical advantages of it.[33–35] van Breemen et al.[35] and Deumel et al.[34] successfully demonstrate a large-array PePD image sensor using thin-film transistor (TFT) based ROICs, but those are limited in their resolution due to the limited minimum feature size in the TFT backplane process. Yi et al.[33] implemented a high-resolution image sensor with a small pixel pitch using a perovskite color converter instead of a photodiode, which has the disadvantages of lower efficiency and reduced sharpness due to diffraction of the converted light. In addition, 3D imaging has been successfully demonstrated using fast-responding PePD by directly measuring the travel time of light reflected from the object by using a single PePD and scanning across the scene.[32] Meanwhile, other thin-film material-based PDs have been monolithically integrated on Si CMOS ROIC. e.g., 35 Mpix organic photodiode-based color image sensors[18] and 6 Mpix quantum dot based short-wave infrared image sensors.[36] Despite these attempts, PePD have not been integrated on Si CMOS ROIC, which can bring out the best in perovskites and leads to fast and high-resolution imager.[37–39] To realize this integration, the PePD stack needs to be fabricated on electrode materials that are compatible with Si CMOS technology, e.g., copper (Cu), aluminum (Al), tantalum nitride (TaN), and titanium nitride (TiN). In addition, the PePD needs to be stable under stress like heat and reverse biases, to avoid performance deterioration and breakdown. Cu and Al are reported to degrade the perovskites due to chemical reactions caused by the interdiffusion between the metals and halides, especially under stresses like heat and reverse

biases.[40–43] Thus, TiN is implemented as electrodes in this work for stability concerns.[41] In a reverse biased perovskite solar cell (PSC), the reaction between halide defects and holes injected through C_{60} was reported to degrade the perovskite layer.[44] Passivating the defects and adding hole-blocking layers like high bandgap metal oxides can prevent such degradation.[44] Finally, the PePD's photocurrent response needs to be fast for distance sensing.

In this work, we developed a PePD stack with stable performance at reverse biases, leading to an at least 100 dB linear dynamic range at a voltage between -2 V and -1 V. Moreover, the PePD stack shows a fast carrier transit time of 5.7 ns at -2 V. Such PePD stacks were then monolithically integrated on top of fully processed Si ROICs, the first-of-a-kind to the best of the authors' knowledge, and demonstrated small pixel pitch, high resolution 2D color-imaging. Photodiode top-electrode controlled light demodulation is proposed to exemplify a high resolution iToF image sensor to capture depth information, leading to a 3D imaging that discriminates objects within a sub-meter range.

RESULTS AND DISCUSSION

Perovskite photodiode

To enable 2D and 3D imaging with perovskite absorbers, we developed a PePD stack that can be integrated onto an existing Si CMOS ROIC using TiN as the per pixel PD bottom electrode.[45] With TiN as bottom electrode, nickel oxide (NiO_x), [4-(3,6-Dimethyl-9H-carbazol-9-yl)butyl] phosphonic acid (Me-4PACz), aluminum oxide nanoparticles (Al_2O_3 NPs), perovskite, buckminsterfullerene (C_{60}), zinc oxide (ZnO) and indium tin oxide (ITO) were sequentially deposited following the procedures described in "Methods". Fig.1 shows the stack configuration. The sputtered NiO_x acts as a compact electron-blocking and hole-transporting material (Fig. 1(b)).

A thin layer of Me-4PACz significantly modifies the energy level of NiO_x surface, changing the valance band maximum energy (E_{VBM}) of the NiO_x surface from -5.06 eV to -5.46 eV,[46] leading to good energetic alignment with the E_{VBM} of the perovskite (Fig. 1(b)). Al_2O_3 NPs were applied to improve the wetting of perovskite solution on the Me-4PACz film. Following our previous work on PSCs, a perovskite solution with a nominal composition of $FA_{0.9}Cs_{0.1}PbI_{2.855}Br_{0.145}$ and an additional 30 mol% (relative to Pb) methylammonium chloride (MACl) was spin coated, followed by annealing, to create a polycrystalline perovskite film with an average crystal size of 700 nm.[47] Especially, both buried and top interfaces of the perovskite layer were treated with 2-thiopheneethylammonium chloride (TEACl) to reduce defect density and improve the energy alignment between the perovskite and carrier transport layers.[47] C_{60} and an additional high bandgap ZnO layer provide electron-transporting and hole-blocking functions (Fig. 1 (b)). Finally, ITO is applied on top as transparent contact. This stack shows a good stability. When biased at -2 V in darkness for 30 min, EQE and J_{dark} remain almost unchanged (Fig. S1).

This stack delivers constant EQE and photocurrent below -0.7 V (Fig. 1(c, d)). A constant EQE, thus photocurrent, across a range of reverse biases is critical for high quality 2D imaging with photocurrent integration. The dark current density (J_{dark}) of the PePD is below 5×10^{-7} A/cm^2 when the bias (V) is between 0 and -2 V (Fig. 1 (d)). Though the J_{dark} at a low reverse bias, e.g. at -0.5 V, is higher than the lowest reported values in the literatures,[35,48,49] it is among the lowest reported values when $V \leq$ -1 V.[50,51] This low J_{dark} offers at least 100 dB linear dynamic range (LDR) when $V \leq$ -1 V (Fig. 1 (e)), crucial for linearity in 2D imaging. Though the linearity is lost when $V >$ -1 V, i.e. the EQE, thus photocurrent, reduces to 0 as V approaches forward biases (Fig. 1 (c, d)), this makes it possible to exploit this voltage range to switch the PePD on/off for iToF 3D imaging.

To achieve iToF 3D imaging, the PePD is required to be fast enough to respond to a change of intensity of the incident light. The temporal response of a photodiode is determined by both the carrier transit time τ_{tr}, and the RC constant τ_{RC}, with a limitation set by the slower of the two.[32,52,53] τ_{tr} is the time for the carriers to flow through the whole device stack, while τ_{RC} is the time defined by the product of R by C, where R encompasses the photodiode resistance, contact resistance, and load resistance, and C is the combined capacitance of the photodiode device and the parasitic capacitance of the measurement system.

In this work, we measured a PePD's temporal response by the time-resolved photocurrent (TRPC). To minimize the geometric capacitance of the PePD, we considered a small PePD active area of 625 μm^2. A 532 nm-laser source of 2.3 ns pulse width, 22 $\mu J/cm^2$ energy density, and 20 Hz repetition rate was used to generate carriers in a PePD at voltages 0 V, -0.5 V, -1 V, -1.5 V and -2.0 V, respectively. Under the electric field induced by the built-in potential (V_{bi}) and the external bias (V), the photogenerated electrons and holes drifted toward the respective electrode. The induced TRPC response was recorded using an oscilloscope with a bandwidth of 200 MHz and an input resistor of 50 Ω (Fig. 1 (f)). The response time, defined as the time the photocurrent is reduced from the peak value to 1/e, was extracted through a single exponential fit of the TRPC curves. The τ obtained at 0 V, -0.5 V, -1 V, -1.5 V and -2.0 V is 28.2 ns, 25.1 ns, 23.9 ns, 22.9 ns and 23.4 ns, respectively. A further linear fitting of τ^2over $1/(V+V_{bi})^2$ allows the calculation of τ_{RC} and τ_{tr}, as indicated in the equation in Fig. 1 (g).[32,52,53] The detailed derivations can be found in Note S1. Here we assume V_{bi} = -1 V according to commonly reported values in the literatures.[54–56] In this case, the τ_{RC} is estimated to be 22.2 ns, and τ_{tr} is estimated to be 5.76 ns, 8.6 ns and 17.3 ns at -2 V, -1 V and 0 V, respectively. A τ_{tr} below 6 ns at -2 V approaches the fastest reported τ_{tr} ~ 1 ns in literatures,[32,53] showing state-of-the-art response speed. Even at 0 V, τ_{tr} is below 20 ns,

implying the PePD stack is adequately fast for iToF distance sensing. Although the device area is as small as 625 μm^2, τ_{RC} still dominantly contributes to τ. This suggests that a larger PD would have a longer response time due to larger τ_{RC}. On the contrary, τ can only approach τ_{tr} when the PD active area further shrinks.

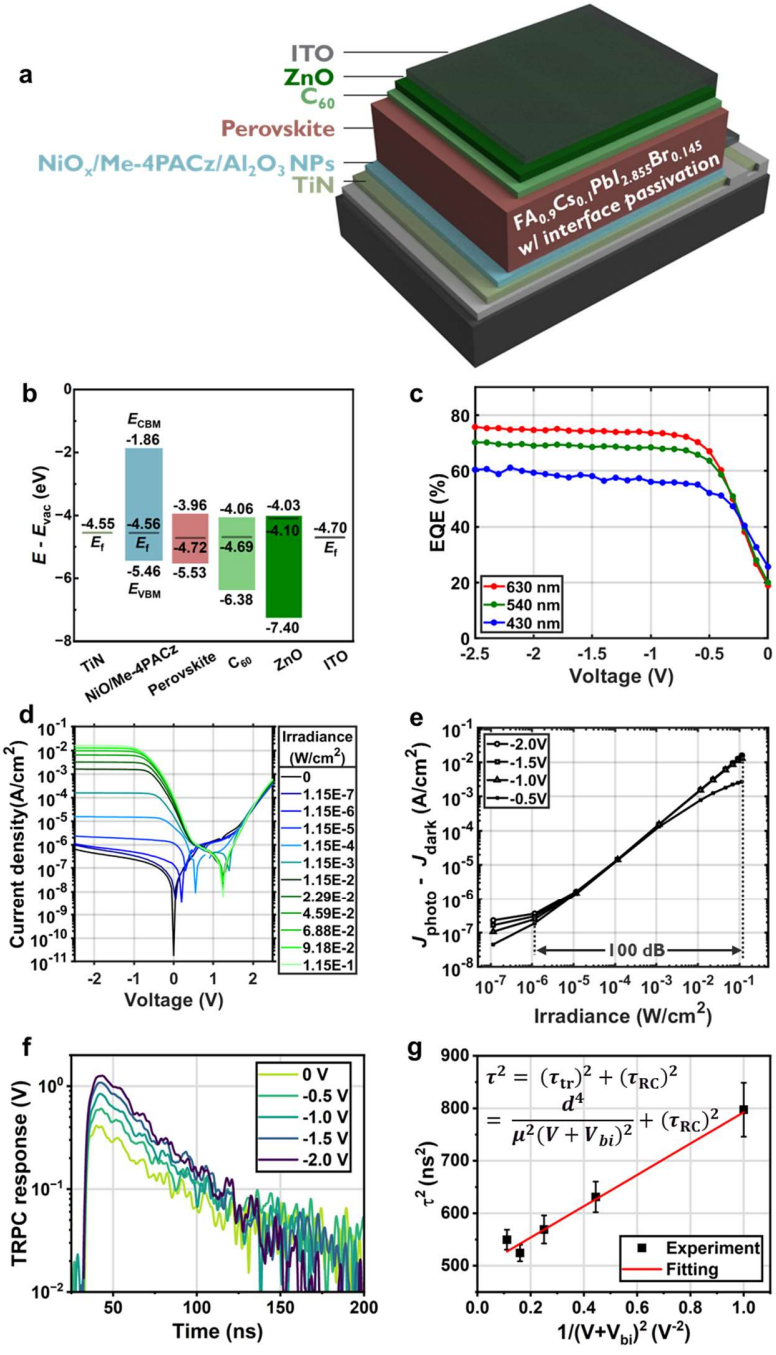

Figure 1: (a) A schematic of the structure of the PePD. (b) E_{CBM}, E_f and E_{VBM} of each layer in the PePD. (c) EQE as a function of voltage, under an illumination with wavelength of 630 nm, 540 nm and 430 nm, respectively. (d) The PePD's current density as a function of voltage in darkness and under white LED light of various irradiances. (e) Linearity plot at −2.0 V, -1.5 V, -1.0 V and -0.5 V, showing the photocurrent density, J_{photo}, minus the dark current density, J_{dark}, as a function of light intensity. The J_{photo} and J_{dark} values are extracted from Fig. 1 (d). (f) The time resolved photocurrent response of a 625 μm^2 stand-alone PePD at 0 V, -0.5 V, -1.0 V, -1.5 V, and -2.0 V. (g) τ^2 as a function of $1/(V+V_{bi})^2$. d represents the thickness of materials between the two PePD electrodes, while μ denotes the average mobility in the PePD.

Integration of PePD on CMOS ROIC

The PePD stack in Fig. 1 (a) was integrated on top of CMOS ROICs comprising 3-transistor (3T)-based pixel arrays in size of 512 × 768. Prototype sensor occupies 6.2×7.53 mm^2 with a pixel pitch of 5 μm. Afterwards, the imager sensors were packed for further characterization (Fig. 2 (a)). The fabrication details of the prototype image sensors can be found in "Methods". To examine whether the PePD was successfully integrated on the ROIC, a high-angle annular dark-field (HAADF) scanning transmission electron microscopy (STEM) and an energy-dispersive X-ray spectroscopy (EDS) were performed on the cross section of the image sensor (Fig. 2). Fig. 2 (b, c, p, q) shows the presence of TiN as the bottom electrode of each pixel, with pixel pitch being 5 μm. All the other stack layers also can be clearly identified by their compositing elements (Fig. 2 (b-r), Fig. S2). Fig. 2 (b, c) show that only vertical grain boundaries are visible in the perovskite layer. The absence of horizontal grain boundaries implies that the charge transport at the vertical direction will not be obstructed by discontinuity of the crystal, supposedly benefiting the fast charge transport. It is noticeable that an ultra-thin layer of SiO_x (Fig. 2 (r, f)) exists between the TiN and

NiO_x. We speculate that this is due to an incomplete chemical-mechanical polishing. As the SiO_x is ultrathin, the electrical behavior of the PePD on this image sensor is not affected, which will be further discussed in the following section. As evidenced by Fig. 2, the PePD stack was successfully integrated onto the ROIC.

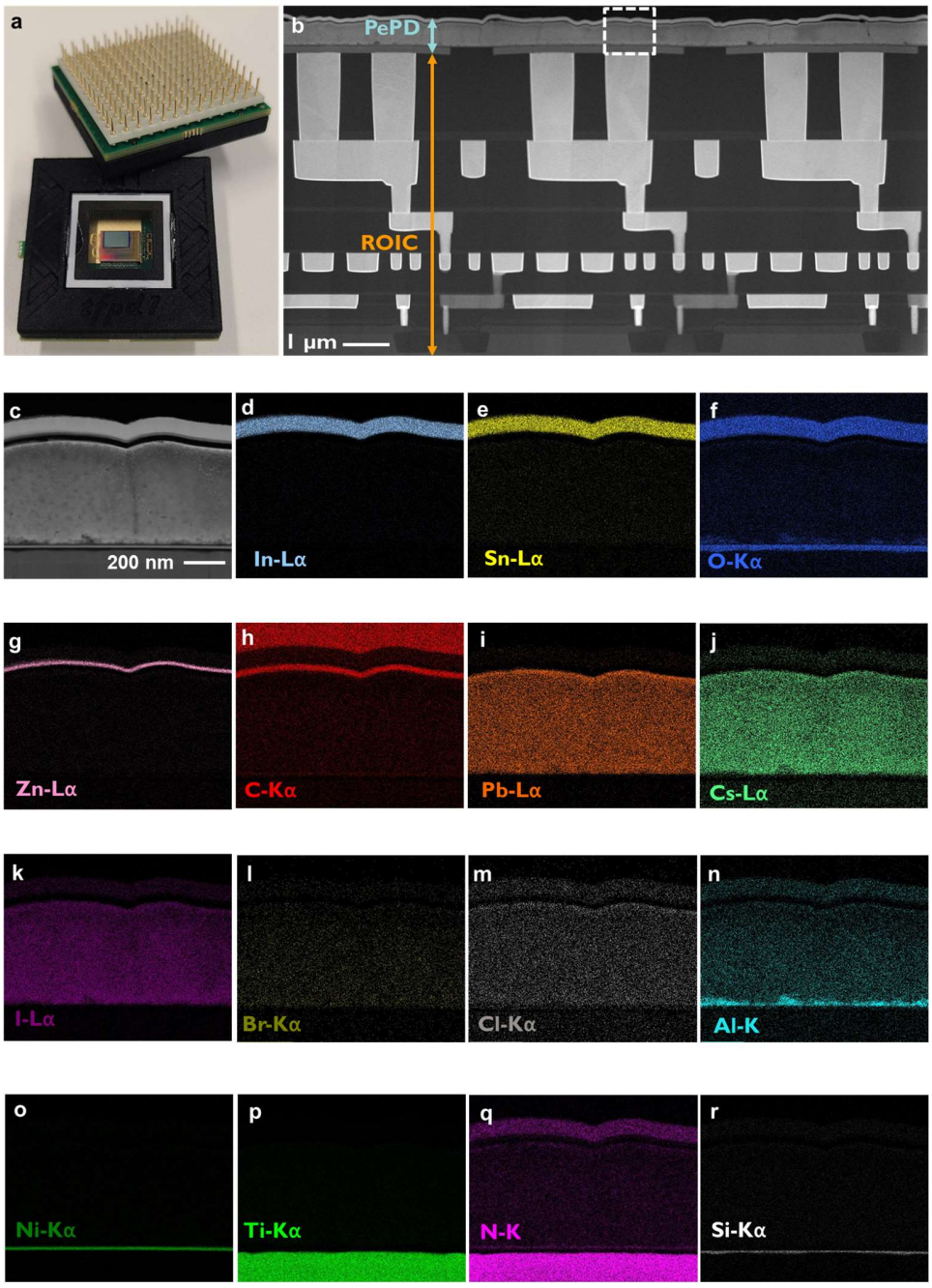

Figure 2: (a) An optical image of bonded and packed image sensors integrating perovskite-based photodiodes. (b) A cross-sectional HAADF STEM image of the image sensor including the Si ROIC and the PePD. (c) A cross-sectional HAADF STEM image of the PePD within the area

marked by the dashed frame in Fig. 2 (b). (d-r) The EDS elemental mapping of In, Sn, O, Zn, C, Pb, Cs, I, Br, Cl, Al, Ni, Ti, N, and Si of the area corresponding to Fig. 2 (c). To note, the carbon EDS signal on top of ITO originates from the spin-on carbon coating. The N signal in the ITO layer originates from the overlap between In-M and N-K signals.

2D imaging demonstration

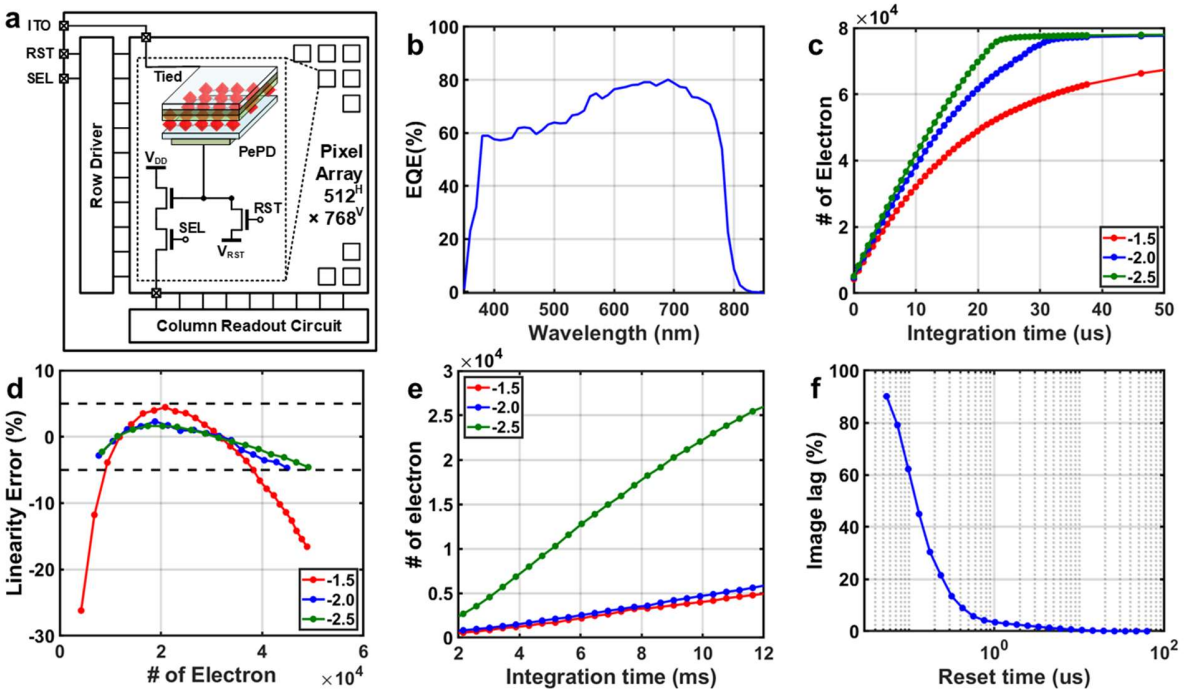

Figure 3: Image sensor performance. (a) Overall architecture. (b) EQE as a function of wavelength for the PePD biased at -2 V. (c) Output curve under white LED light condition with the various PePD bias. (d) Linearity error results of prototype sensor. (e) Output curve under dark condition with various PePD bias voltages. (f) Image lag as a function of reset time duration for the PePD biased at -2 V.

Fig. 3 (a) depicts the overall architecture of the proposed image sensor composed of a 512×768 pixel array with PePD and the basic 3T pixel architecture, a row pixel signal driver at the left side of the pixel array, and a column readout circuit at the bottom. An off-chip analog-to-digital converter (ADC) was adopted for flexibility in the test. The PePD pixel is designed to readout integrated holes while electrons are drained through the top electrode (ITO). To maintain reverse bias for the PePD, the anode of the PePD is reset to 1.8 V throughout the measurements, and the ITO voltage is adjusted to modify the reverse bias of the PePD.

Fig. 3 (b) shows EQE measurement results from the prototype sensor for the PePD biased at −2 V. There are no significant differences between the results from the prototype sensor and the PePD stack, with both reaching approximately 80% at a 700 nm wavelength (Fig. S3). To validate the linearity of the prototype sensor, an output under white LED light condition is measured at the various reverse biases of −2.5 V, −2.0 V and −1.5 V, as plotted in Fig. 3 (c), and the calculated linearity error is depicted in Fig 3 (d). Linearity error calculations follow the standard EMVA 1288[57] and present values at the various reverse biases. It can be seen that the linearity error degrades, especially when it reaches full well capacity (FWC), as the reverse bias decreases. This is because the sensitivity of the PePD decreases when it is less biased (Fig. 1(c)) as more holes are integrated at the anode. The sensor achieves a linearity error of less than ±5% from around 8k to 40k electrons with our optimal bias voltage of −2 V. Even though the linear FWC at −2.5 V is slightly higher than that at −2 V, as shown in Fig. 3 (e), the dark current at −2 V is significantly lower than −2.5 V. Due to this trade-off, we choose the optimal bias point to −2 V during characterization. Fig. 3 (f) demonstrates the image lag of the prototype sensor, revealing a low image lag of 3.4% at 1 μs reset time.

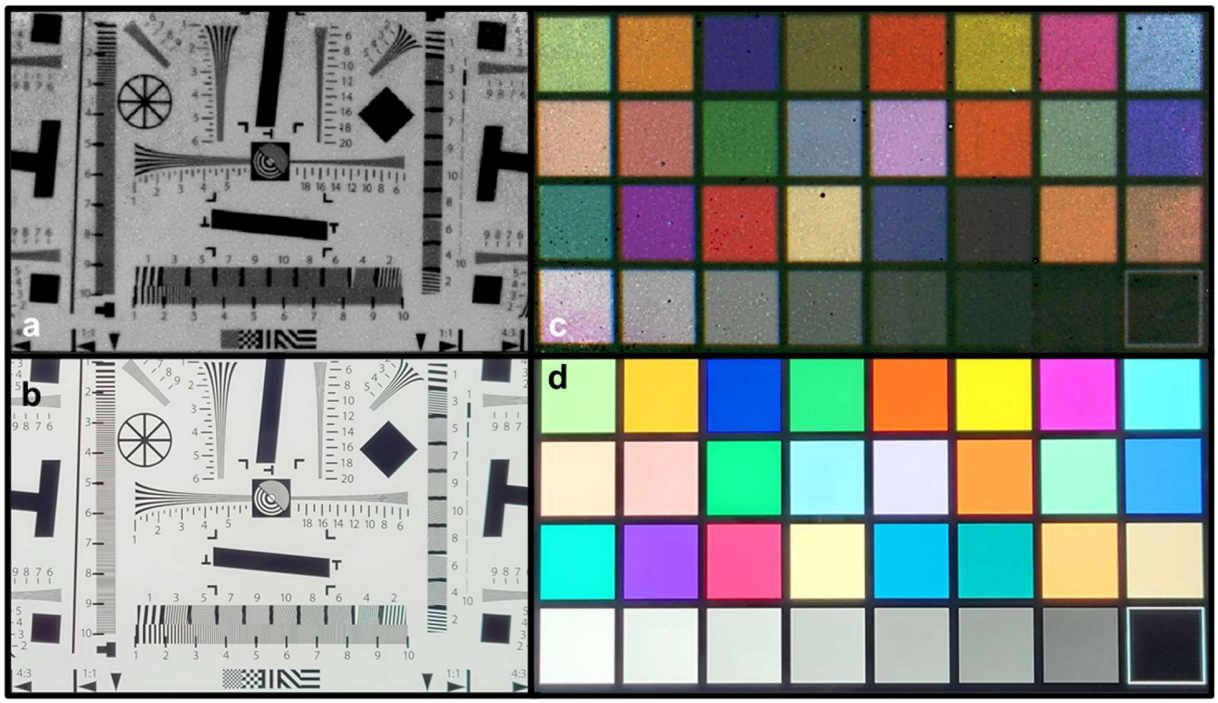

Figure 4: 2D imaging demonstration. Intensity image of resolution chart from (a) prototype sensor and (b) smart phone. Color image of color checker from (c) prototype sensor and (d) smart phone.

Fig. 4 (a) and (b) show the grayscale intensity image of the resolution chart captured by the prototype sensor and the smart phone, respectively. We just adjusted the digital gain and offset, then applied gamma collection to the image from the prototype sensor. Several shapes and gradations on the resolution chart are well-discriminated without requiring further post-processing (Fig. S4). Although the perovskite is not involved in pixelation, spatial resolution of the prototype sensor is enough to distinguish pattern thanks to the high absorption coefficient and low vertical height of perovskite relative to horizontal pixel size[18,37,58,59].

Color images of color checker were also captured using both the prototype sensor and the smartphone as shown in Fig. 4 (c) and (d), respectively. To demonstrate the possibility of color

imaging, the R, G, and B images for the same scene were captured separately using R, G and B color filters respectively, as our prototype sensor does not have in-pixel color filters. Thanks to the flat EQE in almost all operational reverse bias, the color reconstruction process only requires applying the same EQE value to the entire pixel array, without resorting to complex algorithm based on intensity. The integration time for the 2D imaging demonstration was 1.25 ms.

3D imaging demonstration by top electrode controlled iToF operation

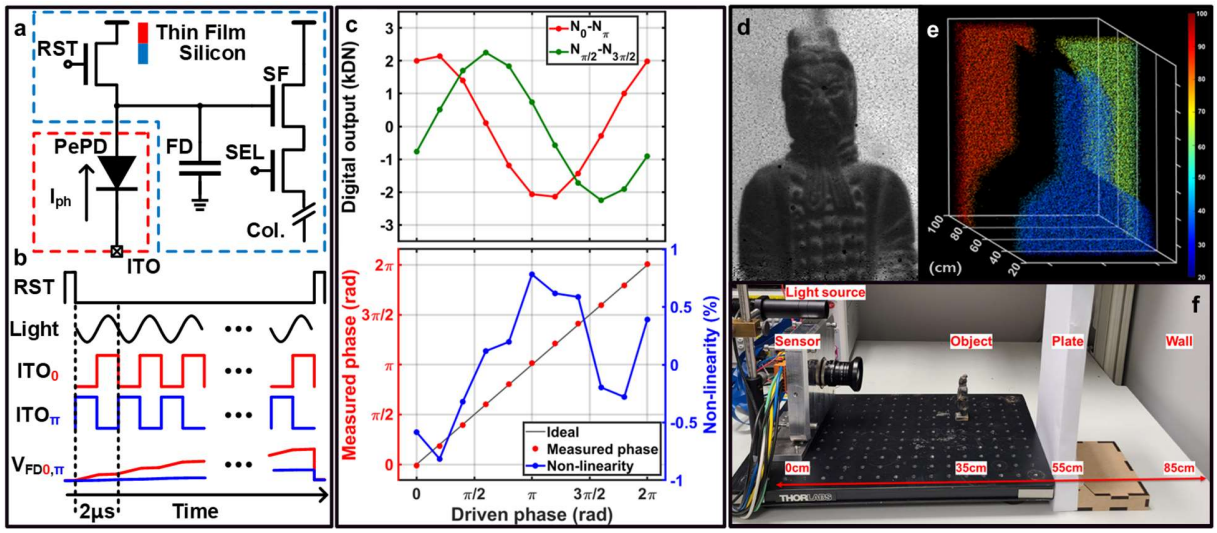

Figure 5: 3D imaging demonstration. Proposed top electrode controlled iToF operation (a) schematics, (b) timing diagram, (c) measured phase difference and non-linearity results with given phase delay. (d) Intensity image and (e) point-cloud depth image captured by the prototype sensor. (f) Measurement setup.

To detect not only intensity of the light but also estimate the distance from the prototype sensor to an object, we adopt the iToF technique to our prototype sensor architecture, which is one of the distance sensing methods (Fig. S5). A light source emits the modulated light with a pre-defined modulation frequency of 500 kHz, which is limited by the large τ_{RC} of the connected pixels, and

the illuminated sensor demodulates the reflected light to find out the phase difference between the emitted light and the received light. In general, a demodulation pixel has two or more taps consisting of: (1) a transfer gate as a switch and (2) a storage node to selectively collect desired phase signal[21,60–63]. However, the classical implementation of the efficient in-pixel transfer gates and storage nodes in the PePD image sensor has not been elaborated. It should also be noted that the classic implementation with additional pixel elements increases the pixel area, which makes high-resolution 3D imaging more difficult.

To overcome this, we propose the top electrode control iToF sensor with basic 3T architecture, without additional in-pixel components, consisting of reset transistor (RST), voltage follower transistor (SF), row select transistor (Sel), storage node generated by parasitic capacitance called as floating diffusion (FD), and photodiode based on the halide perovskite absorber as shown in Fig. 5 (a). The top electrode can be utilized as the transfer gate in the conventional demodulation pixel because the responsivity of the PePD can be controlled by its bias condition (Fig. 1(d)). The designed perovskite stack has high photocurrent in the reverse bias region, while being unresponsive to light at zero or forward bias-regimes. The prototype sensor modulates its EQE by applying a pulse train equal to the optical modulation frequency to the ITO electrode, effectively demodulating the reflected light without the transfer gates.

Fig. 5 (b) depicts the simplified timing diagram of the prototype sensor. For simplicity, two demodulation signals (ITO_0 and ITO_π) with the phase delays of 0 and π rad from the emitted light are illustrated, although two more signals with the phase delays of $\pi/2$ and $3\pi/2$ rad to create quadrature phase information are used in practice. It is essential to collect four data set because two phase data cannot discriminate the distance and reflectance of an object[22]. An extreme case with nearly zero distance is shown to maximize the discrepancy in the voltage domain. The amount

of the accumulate charge is large with the ITO_0 because the reflected light is matched to its high EQE bias, whereas the other ITO_π signal is reversed with the light, generating much less charge. After the integration time between two active high resets, the voltage difference in the FD node is significant. The difference in the V_{FD} with both demodulation signals relies on the distance which produces the phase difference between the reflected light and the ITO_0. Since the phase change is positively proportional to the distance, the V_{FD0} and $V_{FD\pi}$ gradually decreases and increases, respectively, as the distance gets farther from the sensor, allowing us to figure out the depth easily. It is recommended to increase the modulation frequency for improving the depth performance in iToF sensors because the modulation frequency is inversely proportional to depth noise (Fig. S5). Increasing the charge transit speed of the PD is therefore critical to achieve high depth accuracy. Thanks to the high-speed transient response within 6 ns (Fig. 1 f) of our PePD, 3D imaging with high depth accuracy is possible.

As mentioned earlier, four frames data with the phase delays of 0, $\pi/2$, π, and $3\pi/2$, is obtained by the developed PePD image sensor to construct a depth scene. Unlike conventional iToF pixels, the proposed top electrode modulated pixel supports only a single tap, providing (1) less components and (2) tap-mismatch free depth data[60,62], whereas it is needed to capture multiple frames to calculate a depth map. This inevitably causes motion artifacts when measuring moving objects. On the other hand, in our prototype sensor, the whole pixel array is connected, limiting the modulation frequency due to its large capacitance. The capacitance can be significantly reduced by pixelating the PePD stack by row- or column- or even pixel-wise. A sub-μm pitch perovskite patterning is demonstrated by using Electron-beam writing,[64] and direct laser ablation[65], which would fulfil our pixelation needed for higher speed modulation. Moreover, it is also possible to

adopt multi-phase demodulation schemes with isolated ITO electrode, for motion artifact suppression without increasing the number of taps[60,62,66–68].

A light source with a commercial 530-nm wavelength LED and driver was employed to characterize depth performance of the prototype sensor. The upper figure in Fig. 5 (c) plots the voltage differences of V_{FD0}-$V_{FD\pi}$ and $V_{FD\pi/2}$-$V_{FD3\pi/2}$ in the digital domain, called in- and quadrature- phase data, respectively, to extract the phase information by using the arctangent function (Fig. S5). To maintain the intensity of the reflected light, a constant distance is measured by the emitted light with intentionally applied various phase delays of from 0 to 2π, clearly retrieving both sinusoidal with π/2-phase difference similar with ideal calculation (Fig. S6). The lower figure in Fig. 5 (c) shows the ground truth and measured depth as phase delay with a nonlinearity of less than 0.82%, which is normalized by the maximum phase value thanks to tap mismatch free configuration. Fig. 5 (d) and (e) show the intensity and point-cloud depth image captured by the prototype sensor. Objects placed at 35cm, 55cm and 85cm are clearly distinguishable. Our measurement setup is depicted in Fig. 5 (f).

Table 1 and Table S1 summarize the measured characteristics of the prototype PePD sensor and comparison with published state-of-the-art thin-film based image sensors.

Table 1: Measured characteristics of this work compared with published state-of-the-art.

	Readout chain type	Pixel pitch (μm)	Resolution	Rise time (ns)	Fall time (ns)	3D imaging method	Note *
This work	Si 3T	5	768 × 512	NA	5.76*	iToF	25 μm pitch result, V_{bias}=-2V
2022 Najarian[32]	NA	NA	1	< 0.1	0.2	dToF	
2023 Yi[33]	Si CCD*	2.5	4000 × 5600	NA	NA	Structured light	PePD adopted as filter
2018 Xue[69]	NA	5000 (H) 3500 (V)	10 × 10	4×10^5	23×10^5	No	
2021	TFT	38	640 × 480	2700	2300	No	Flexible large area

van Breemen[35]							
2021 Deumel[34]	TFT	50	640 × 480	NA	NA	No	
2019 Zhu[70]	NA*	1000	6 × 6	90	2270	No	Metal/Si-substrate-based pixel
2023 Hou[71]	NA	33	32 x 32	1,290,000	1,370,000	No	Stacked R/G/B color imaging
2023 Liu[72]	NA*	NA	1 x 4	5,200,000	11,000s	No	256 x 256 imaging by scanning
2023 Tang[73]	In_2O_3 TFT	1250*	16 x 16	46,000,000	NA	No	Total area of 2 cm^2 with 16x16 array Photoconductor
2023 Wang[74]	NA	250*	10 x 10	NA	NA	No	Flexible substrate Photodiode size 100x100 μm^2

CONCLUSION AND OUTLOOK

In this study, we engineered a PePD stack that exhibits stable performance under reverse biases, achieving a linear dynamic range of at least 100 dB within a voltage range of -2 V to -1 V. The PePD also demonstrates a swift carrier transit time of 5.7 ns at -2 V. This PePD stack was subsequently integrated directly onto a fully processed Si CMOS ROIC using a 130-nm technology node. This integration resulted in a PePD-based image sensor with a 5-µm pixel pitch and resolution of 512 × 768 pixels, a pioneering achievement as per our understanding. This prototype image sensor demonstrates 80% EQE, a linearity error of less than ±5% from around 20k to 60k electrons, revealing a low image lag of 3.4% at 1 µs reset time at reverse bias of -2 V. It successfully demonstrated high-resolution 2D color-imaging. Furthermore, by manipulating the voltage of the photodiode's top electrode using a basic 3-transistor pixel architecture, the image sensor can function as a 3D sensor, enabling 3D imaging that can differentiate objects within a sub-meter range. Our work presents perovskites as a promising absorber for 2D color imaging and 3D iToF imaging.

Looking ahead to the future, to further increase the ranging resolution, reducing τ_{RC} of the connected pixels are necessary.-Engineering PePD stack materials and patterning PePD to reduce the connected number of pixels would help reduce RC constant, which will allow the image sensor to approach its theoretical modulation frequency limit. Even higher resolution imagers with a smaller pixel pitch, which also helps to reduce the RC time constant, should be relatively easy to achieve by monolithically integrating PePD on Si ROIC, as it has a similar area advantage to 3D stacking, which separates the photo-absorption and readout circuit areas. In addition, near infrared (NIR) light of wavelength like 850 nm and 940 nm is often used for ToF sensing and imaging. Sn-base or Sn-Pb mixed cation-based perovskites allow light absorption up to 1050 nm. Such perovskite absorbers can deliver higher EQE and faster charge collection than Si in NIR, thus very promising to be used in iToF NIR 3D imager.

METHODS

Materials

[4-(3,6-Dimethyl-9H-carbazol-9-yl)butyl] phosphonic acid (Me-4PACz), lead iodide (PbI_2) and cesium iodide (CsI) were purchased from Tokyo Chemical Industry (TCI). MACl was purchased from Shanghai MaterWin. Formamidinium chloride (FACl), formamidinium iodide (FAI) and TEACl were purchased from Greatcell Solar Materials. Fullerene-C_{60} was purchased from Nano-C. Lead bromide ($PbBr_2$), anhydrous 1-butanol, acetonitrile, anhydrous dimethylformamide (DMF), anhydrous 1-methyl-2-pyrrolidone (NMP), anhydrous ethanol, anhydrous isopropanol alcohol (IPA) and Al_2O_3 nanoparticle (NP) dispersion were purchased from Sigma Aldrich. Nickel, ZnO and ITO sputter targets used in magnetron sputtering were obtained from Angstrom

Engineering Inc. Absolute acetone and isopropanol were purchased from VWR. All materials were used as received.

Fabrication of stand-alone PePDs

The Si wafers with stand-alone photodiodes designs were manufactured in a semiconductor line. At the end of the manufacturing, they were covered with photoresist as protection. The wafers were then diced into 3 cm × 3 cm square-shape substrates, and later transferred to labs for the photodiode processing.

To remove the photoresist, these substrates were first ultrasonic cleaned in absolute acetone for 45 min at 50 ℃. To further clean the substrates, they were ultrasonic cleaned in absolute isopropanol for 15 min 50 ℃. , and eventually blow-dried using a nitrogen gun.

Afterwards, the cleaned substrates were transferred into a high-vacuum chamber (base pressure $10^{-7} \sim 10^{-8}$ Torr), in a Nebula system from Angstrom Engineering Inc.15 nm-thick NiO_x films were deposited by reactive sputtering of metallic nickel target using oxygen plasma. The NiO_x films were then annealed in air at 300 °C for 5 min. After cooling, the substrates with NiO_x were transferred to a nitrogen-filled glovebox for the spin-coatings of Me-4PACz, Al_2O_3 NPs, TEACl, perovskite, FACl, and TEACl in sequence:

1) The Me-4PACz solution (1 mmol/L in anhydrous ethanol) was spin-coated on NiO_x at a speed of 3000 rpm for 30 s, followed by annealing at 100 ℃ for 10 min.
2) The Al_2O_3 NP dispersion was diluted 40 times with anhydrous 1-butanol and then sonicated for 10 min at 30 ℃ before use. The diluted Al_2O_3 NP dispersion was spin-coated on the samples at a speed of 3000 rpm for 30 s, immediately followed by annealing at 100 °C for 10 min.

3) Afterwards, the TEACl solution (1.0 mg/mL in anhydrous IPA) was spin-coated at a speed of 3000 rpm for 30 s, followed by annealing at 100 °C for 10 min.
4) The perovskite solution was made by dissolving 418 mg FAI, 70.2 mg CsI, 71.8 mg $PbBr_2$, 54.7 mg MACl and 1145 mg PbI_2 in 2.0 mL mixed solvents of DMF and NMP, with a volume ratio of 9:1. The diluted perovskite precursor solution was stirred overnight at room temperature and diluted to 1.2 M prior to spin-coating. The perovskite precursor solution was dynamically spun onto the substrates and followed by a nitrogen quenching process for 30 s. Then, the perovskite films were annealed at 120 °C for 70 min.
5) The FACl solution (0.5 mg/mL in anhydrous IPA) was dynamically spin-coated onto the perovskite films at a speed of 3000 rpm for 30 s, followed by annealing at 120 °C for 25 min.
6) Then the films were further treated by the TEACl. The TEACl solution (1.0 mg/mL in anhydrous IPA) was dynamically spin-coated at a speed of 3000 rpm for 30 s, followed by annealing at 110 °C for 3 min.

Afterwards, the samples were transferred into high-vacuum chambers (base pressure $10^{-7} \sim 10^{-8}$ Torr), in a Nebula system from Angstrom Engineering Inc. 20 nm C_{60} was thermally evaporated at a rate of 0.5 Å/s. Subsequently, 15 nm ZnO and 70 nm ITO were deposited through linear magnetron sputtering in the same tool.

Fabrication of image sensors

The Si wafers with CMOS ROIC designs were fabricated using a 130-nm-node semiconductor cleanroom line. At the end of the manufacturing, they were covered with photoresist as protection. The wafers were diced into 2.3 cm × 2.9 cm rectangle-shape substrates, which contain multiple test vehicles. The substrates were later transferred to labs for the photodiode processing.

The substrate cleaning and the photodiode stack processing follow the same procedures as described in the fabrication of stand-alone photodiodes. To note, to prevent material deposition on the Al input/output (I/O) pads, which later were used for bonding, metal masks were used during the sputtering and evaporation of charge transport layers, i.e. NiO_x, C_{60}, ZnO, and ITO. For the same reason, to expose the Al pads, after the spin coatings of Me-4PACz, TEACl, perovskite, FACl, and TEACl, the Al pads were cleaned with DMF to remove these materials. In the end, the image sensor test vehicles were laser-diced from the substrates, and then bonded onto customized printed circuit boards, followed by gluing spacers and protecting glasses on top of the image sensors.

Ultraviolet photoelectron spectroscopy (UPS)

The energy band diagram of ZnO is deduced from valence band spectra of isolated films on gold coated Si substrate by UPS. The UPS measurements were performed using a PHI 5000 VersaProbe system from Physical Electronics equipped with a He I (21.2 eV) UV source. The spectrometer was calibrated with Ag foil and all samples were sputter cleaned using a gas cluster ion beam (GCIB) at 2.5 kV energy/atom. Post-processing of spectra was carried out using MultiPak (data reduction software for XPS and AES by ULVAC-PHI).

STEM and EDS

Before STEM, a spin-on-carbon capping layer was deposited on top of the imager and subsequently baked at 75 °C for 10 min. Afterwards, a Pt capping layer was deposited using a Ga-ion beam in a FEI Helios 450 dual beam microscope. In-situ lift out and thinning of a cross section is performed using focused ion beam (FIB). STEM and EDS are performed at 200 kV using Titan3 G2 60-300.

Standalone PePD characterizations

The current–voltage (*I–V*) of the PePD in darkness and under illumination were measured in pulsed *I-V* mode in a N_2-filled glovebox, using a Paios all-in-one system by Fluxim. The illumination source is a white LED. The current as a function of time in Fig. S1 was recorded using a Keithley 2602A source-measure unit.

The EQE spectra were recorded on a Stanford Research System model SR830 lock-in amplifier unit coupled with a monochromator and a 150 W halogen lamp (OSRAM HLX 64633). The signal was first amplified by a Stanford Research System SR570 low-noise current preamplifier. A calibrated Si photodiode with a known spectral response was used as a reference.

The TRPC measurement was performed using a probe station. One probe was connected to a Keithley source meter to bias the sample with constant voltages. The generated photocurrent from a PePD with 625 μm^2 active area was collected by the second probe connected to a FEMTO HSA-Y-1-60 high speed amplifier with a fixed gain of 60 dB. A Keysight DSOX3024T oscilloscope with 200MHz bandwidth was connected using a 50 Ω coaxial cable to record the photocurrent signals. A Q switched laser (CryLas FTSS-355-300) was used as a light source. The sample was optically pumped by doubled frequency pulses of 532 nm wavelength with 2.3 ns (FWHM) pulse width at a repetition rate of 20 Hz. The laser beam was focused on the sample into a Gaussian spot of 367 μm (FWHM) using a Mitutoyo 10X infinity corrected objective with focal length of 20 mm and 0.28 numerical aperture.

2D Imaging Characterization and demonstration

The PePD image sensors were characterized by a custom-made printed circuit board with packaged chips. The printed circuit board integrated off-chip ADCs (AD5648ARUZ-2) and field-

programmable gate arrays (CYUSB3014-BZXI). The output of the ADC is connected to a PC to be saved. DC power is applied by AGT N6705A power analyzer. The EQE spectrum was obtained in the same procedure as that using the standalone PePDs. The transient photo response output curve was measured under direct light provided by a white LED (HPD2 series dome light) and under dark condition. All data came from the ROI (300×300 at the center of array). Image lag was recorded with direct light provided by a white LED (HPD2 series dome light) to saturate photo diode and sweep reset time to verify the amount of residue charge in photodiode.

For the 2D Imaging demonstration, optical lens was adopted as C-mount lens (LM8HC-SW). SDCV-3500 image viewer generated scene with resolution chart (TE170) and color checker (TE226). Image viewer was set at 60 cm distance from the sensor and the integration time was 1.25 ms. For the grey-scale demonstration, we applied dark point calibration, photo response non-uniformity calibration, fixed pattern noise calibration, 1st order calibration containing digital gain and offset calibration, and gamma correction. For the color demonstration, we took the 3 images with R, G, and B filter (FDIR, FGV9M, FGB25M from Thorlabs) and divided average EQE value of each wavelength to whole array and demosaicing color image thanks to flat EQE value under diverse reverse bias region.

The smartphone used for comparison was a Galaxy S20+, which has 64M pixel with 1.8μm pixel pitch. Fig. 4 (b) was taken under F/1.8, 26mm focal length, 1693×1093 (1.85Mp) pixel resolution. Fig. 4 (d) was taken under F/1.8, 26mm focal length, 759×422 (0.32Mp) pixel resolution.

3D Imaging Demonstration

For the 3D Imaging demonstration, the modulation signal was generated by a AGT81130A pulse generator. A Thorlabs M530L3 530 nm LED was adopted for emitting light which was modulated

by pulse signals from a Thorlabs DC2200 LED driver. The trigger signal related to the modulation pulse came from the chip to the pulse generator, which generated the ITO control signal and the light source driving signal to synchronize them.

To verify the demodulation operation, we illuminated the sensor directly from the LED without changing the distance while changing the delay of light trigger to avoid input level difference due to the distance. The delay step is expressed in units of the modulation frequency phase i.e. 0.2π and a total of 11 sampling points from 0 to 2π are measured. The modulation frequency was 500kHz and the integration time was 12.5 ms. Averaging the data of 100 frames was used to remove noise at each sampling point.

The depth image was taken with three objects: doll, white plane, and wall. Objects were located 35, 55, 85 cm respectively. Modulation frequency was 500kHz and integration time was 12.5 ms. Averaging over 50k frame data was used to remove noise. The ROI was set to 300×260 pixels in the center of the array and we applied 1^{st} order calibration to raw depth data.

ASSOCIATED CONTENT

Supporting information

The supporting information contains photodiode stability data, supplementary EQE data, calculation method of RC constant and carrier transit time, TEM images, Comparison of imager characteristics between this work and the other publications, modulation transfer function results, iToF working principles, and calculation of integrated charges.

AUTHOR INFORMATION

Corresponding Author

Jiwon Lee*, email: jiwonlee@postech.ac.kr

Jan Genoe*, email: jan.genoe@imec.be

Author contributions

W.S. and J.K. developed and characterized PePDs and the image sensors and prepared the manuscript draft. K.E. and S.H. contributed to TRPC measurement and analysis. X.Z., I.P.M., S.S., Y.K. contributed to photodiode stack development and device physics analysis. A.B.S. contributed to UPS measurement and analysis. P.C. contributed to STEM and EDS measurement and analysis. F.D.R. and E.V. contributed to the dicing and packaging of the image sensors. N.C. contributed to post processing of ROIC backplane. J. H. K., R.G., S.-J.K., J.L, and J.G contributed to the analysis of the scientific data and supervised the work.

ACNOWLEDGEMENT

Part of this work received financial support from the Fund for Scientific Research Flanders (FWO) under Project number S004322N (GigaPixel).

REFERENCE

(1) Yokogawa, S.; Oshiyama, I.; Ikeda, H.; Ebiko, Y.; Hirano, T.; Saito, S.; Oinoue, T.; Hagimoto, Y.; Iwamoto, H. IR Sensitivity Enhancement of CMOS Image Sensor with Diffractive Light Trapping Pixels. *Sci Rep* **2017**, *7* (1), 1–9. https://doi.org/10.1038/s41598-017-04200-y.

(2) McGrath, D.; Tobin, S.; Goiffon, V.; Magnan, P.; Roch, A. Le; Tobin, S.; Goiffon, V.; Magnan, P.; Roch, A. Le. Dark Current Limiting Mechanisms in CMOS Image Sensors. *Electronic Imaging* **2018**, *30*, 1–8. https://doi.org/10.2352/ISSN.2470-1173.2018.11.IMSE-354.

(3) Oh, Y.; Lim, J.; Park, S.; Yoo, D.; Lim, M.; Park, J.; Kim, S.; Jung, M.; Kim, S.; Lee, J.; Baek, I. G.; Ryu, K.; Kim, K.; Jang, Y.; Keel, M. S.; Bae, G.; Yoo, S.; Jeong, Y.; Kim, B.; Ahn, J.; Lee, H.; Yim, J. A 140 DB Single-Exposure Dynamic-Range CMOS Image Sensor with In-Pixel DRAM Capacitor. *Technical Digest - International Electron Devices Meeting, IEDM* **2022**, *2022-December*, 3771–3774. https://doi.org/10.1109/IEDM45625.2022.10019558.

(4) Iida, S.; Sakano, Y.; Asatsuma, T.; Takami, M.; Yoshiba, I.; Ohba, N.; Mizuno, H.; Oka, T.; Yamaguchi, K.; Suzuki, A.; Suzuki, K.; Yamada, M.; Takizawa, M.; Tateshita, Y.; Ohno, K. A 0.68e-Rms Random-Noise 121dB Dynamic-Range Sub-Pixel Architecture CMOS Image Sensor with LED Flicker Mitigation. In *2018 International Electron Devices Meeting (IEDM)*; IEEE, 2018; Vol. 2018-December, pp 10.2.1-10.2.4.

(5) Thomas, S. Imaging Pixels Squeeze In. *Nat Electron* **2023**, *6* (12), 927. https://doi.org/10.1038/s41928-023-01103-x.

(6) Liqiang, H.; Yao, S.; Theuwissen, A. J. P. A Charge Transfer Model for CMOS Image Sensors. *IEEE Trans Electron Devices* **2016**, *63* (1). https://doi.org/10.1109/TED.2015.2451593.

(7) Kato, Y.; Sano, T.; Moriyama, Y.; Maeda, S.; Yamazaki, T.; Nose, A.; Shiina, K.; Yasu, Y.; Van Der Tempel, W.; Ercan, A.; Ebiko, Y.; Van Nieuwenhove, D.; Sukegawa, S. 320×240 Back-Illuminated 10-Mm CAPD Pixels for High-Speed Modulation Time-of-Flight CMOS Image Sensor. *IEEE J Solid-State Circuits* **2018**, *53* (4), 1071–1078. https://doi.org/10.1109/JSSC.2018.2789403.

(8) Van Sieleghem, E.; Karve, G.; De Munck, K.; Vinci, A.; Cavaco, C.; Suss, A.; Van Hoof, C.; Lee, J. A Backside-Illuminated Charge-Focusing Silicon SPAD with Enhanced Near-Infrared Sensitivity. *IEEE Trans Electron Devices* **2022**, *69* (3), 1129–1136. https://doi.org/10.1109/TED.2022.3143487.

(9) Genoe, J.; Coppée, D.; Stiens, J. H.; Vounckx, R. A.; Kuijk, M. Calculation of the Current Response of the Spatially Modulated Light CMOS Detector. *IEEE Trans Electron Devices* **2001**, *48* (9), 1892–1902.

(10) Iwabuchi, S.; Maruyama, Y.; Ohgishi, Y.; Muramatsu, M.; Karasawa, N.; Hirayama, T. A Back-Illuminated High-Sensitivity Small-Pixel Color CMOS Image Sensor with Flexible Layout of Metal Wiring. In *IEEE International Conference on Solid-State Circuits (ISSCC)*; 2006.

(11) Park, J.; Lee, Y.; Kim, B.; Kim, B.; Park, J.; Yeom, E.; Jung, Y.; Kim, T.; Yoon, H.; Kim, Y.; Park, J.; Moon, C.-R.; Park, Y. Pixel Technology for Improving IR Quantum Efficiency of Backside-Illuminated CMOS Image Sensor. In *International Image Sensor Workshop*; 2019.

(12) Skorka, O.; Micinski, S.; Perkins, A.; Gravelle, B.; Li, X.; Ispasoiu, R. 1.4 Mm Pixel, 8 MP, > 5 Mm Epi, RGB-IR Image Sensor. In *IISW*; 2023.

(13) Ispasoiu, R.; Skorka, O.; Kumar, A.; Gopalakrishna, S.; Desai, R.; Gravelle, R.; Li, X.; Tekleab, D. Image Sensor Family with 1.40 Mm Pixel, 10ke-LFW, NIR-Enhanced QE, Extended Dynamic Range, and Low Power Consumption. In *IISS*; 2023.

(14) Keel, M. S.; Kim, D.; Kim, Y.; Bae, M.; Ki, M.; Chung, B.; Son, S.; Lee, H.; Jo, H.; Shin, S. C.; Hong, S.; An, J.; Kwon, Y.; Seo, S.; Cho, S.; Kim, Y.; Jin, Y. G.; Oh, Y.; Kim, Y.; Ahn, J. C.; Koh, K.; Park, Y. A 4-Tap 3.5 Mm 1.2 Mpixel Indirect Time-of-Flight CMOS Image Sensor with Peak Current Mitigation and Multi-User Interference Cancellation. In *IEEE International Solid-State Circuits Conference [ISSCC]*; Institute of Electrical and Electronics Engineers Inc., 2021; Vol. 64, pp 106–108. https://doi.org/10.1109/ISSCC42613.2021.9365854.

(15) Keel, M. S.; Kim, D.; Kim, Y.; Bae, M.; Ki, M.; Chung, B.; Son, S.; Lee, H.; Shin, S. C.; Kye, M.; An, J.; Kwon, Y.; Seo, S.; Cho, S.; Kim, Y.; Jin, Y. G.; Oh, Y.; Kim, Y.; Ahn, J.; Lee, J. A 1.2-Mpixel Indirect Time-of-Flight Image Sensor with 4-Tap 3.5-Mm Pixels for Peak Current Mitigation and Multi-User Interference Cancellation. *IEEE J Solid-State Circuits* **2021**, *56* (11), 3209–3219. https://doi.org/10.1109/JSSC.2021.3112405.

(16) Colace, L.; Assanto, G. Germanium on Silicon for Near-Infrared Light Sensing. *IEEE Photonics J* **2009**, *1* (2), 69–79. https://doi.org/10.1109/JPHOT.2009.2025516.

(17) IEDM. High-Definition Visible-SWIR InGaAs Image Sensor Using Cu-Cu Bonding of III-V to Silicon Wafer; IEEE, 2019.

(18) Nishimura, K.; Shishido, S.; Miyake, Y.; Yanagida, M.; Satou, Y.; Shouho, M.; Kanehara, H.; Sakaida, R.; Sato, Y.; Hirase, J.; Tomekawa, Y.; Abe, Y.; Fujinaka, H.; Matsunaga, Y.; Murakami, M.; Harada, M.; Inoue, Y. An 8K4K-Resolution 60fps 450ke--Saturation-Signal Organic-Photoconductive-Film Global-Shutter CMOS Image Sensor with in-Pixel Noise Canceller. In *Digest of Technical Papers - IEEE International Solid-State Circuits Conference*; Institute of Electrical and Electronics Engineers Inc., 2018; Vol. 61, pp 82–84. https://doi.org/10.1109/ISSCC.2018.8310194.

(19) Royo, S.; Ballesta-Garcia, M. An Overview of Lidar Imaging Systems for Autonomous Vehicles. *applied sciences* **2019**, *9*, 4093. https://doi.org/10.3390/app9194093.

(20) Kim, S. J.; Han, S. W.; Kang, B.; Lee, K.; Kim, J. D. K.; Kim, C. Y. A Three-Dimensional Time-of-Flight CMOS Image Sensor with Pinned-Photodiode Pixel Structure. *IEEE Electron Device Letters* **2010**, *31* (11), 1272–1274. https://doi.org/10.1109/LED.2010.2066254.

(21) Kim, S. J.; Kim, J. D. K.; Kang, B.; Lee, K. A CMOS Image Sensor Based on Unified Pixel Architecture with Time-Division Multiplexing Scheme for Color and Depth Image Acquisition. *IEEE J Solid-State Circuits* **2012**, *47* (11), 2834–2845. https://doi.org/10.1109/JSSC.2012.2214179.

(22) Lange, R. *3D Time-of-Flight Distance Measurement with Custom Solid-State Image Sensors in CMOS/CCD-Technology*.

(23) Piao, C.; Ahn, Y.; Kim, D.; Park, J.; Kang, J.; Kim, S. J.; Chun, J. H.; Choi, J. A Low-Power Indirect Time-of-Flight CMOS Image Sensor With Fixed Depth Noise Compensation and Dual-Mode

Imaging for Depth Dynamic Range Enhancement. *IEEE Transactions on Circuits and Systems I: Regular Papers* **2022**, *69* (10), 3989–3999. https://doi.org/10.1109/TCSI.2022.3188045.

(24) Hatakeyama, K.; Okubo, Y.; Nakagome, T.; Makino, M.; Takashima, H.; Akutsu, T.; Sawamoto, T.; Nagase, M.; Noguchi, T.; Kawahito, S. A Hybrid ToF Image Sensor for Long-Range 3D Depth Measurement Under High Ambient Light Conditions. *IEEE J Solid-State Circuits* **2023**, *58* (4), 983–992. https://doi.org/10.1109/JSSC.2023.3238031.

(25) Park, Y.; Kang, J.; Park, D.; Son, I.; Hwang, J.-H.; Kim, S.-J. A 160×120 Indirect Time-of-Flight Sensor with Pixel-Level Adaptive ΔΣ-Operations for Background Light Cancellation. In *2023 Asian Conference on Solid-State Circuits (ASSCC)*; IEEE, 2023; pp 19.1.1-19.1.3.

(26) Green, M. A.; Ho-Baillie, A.; Snaith, H. J. The Emergence of Perovskite Solar Cells. *Nat Photonics* **2014**, *8* (7), 506–514. https://doi.org/10.1038/nphoton.2014.134.

(27) Yin, W. J.; Shi, T.; Yan, Y. Superior Photovoltaic Properties of Lead Halide Perovskites: Insights from First-Principles Theory. *Journal of Physical Chemistry C* **2015**, *119* (10), 5253–5264. https://doi.org/10.1021/jp512077m.

(28) Stranks, S. D.; Eperon, G. E.; Grancini, G.; Menelaou, C.; Alcocer, M. J. P.; Leijtens, T.; Herz, L. M.; Petrozza, A.; Snaith, H. J. Electron-Hole Diffusion Lengths Exceeding 1 Micrometer in an Organometal Trihalide Perovskite Absorber. *Science (1979)* **2013**, *342* (6156), 341–344. https://doi.org/10.1126/science.1243982.

(29) Yang, Z.; Yu, Z.; Wei, H.; Xiao, X.; Ni, Z.; Chen, B.; Deng, Y.; Habisreutinger, S. N.; Chen, X.; Wang, K.; Zhao, J.; Rudd, P. N.; Berry, J. J.; Beard, M. C.; Huang, J. Enhancing Electron Diffusion Length in Narrow-Bandgap Perovskites for Efficient Monolithic Perovskite Tandem Solar Cells. *Nat Commun* **2019**, *10* (1), 4498. https://doi.org/10.1038/s41467-019-12513-x.

(30) Yang, X.; Fu, Y.; Su, R.; Zheng, Y.; Zhang, Y.; Yang, W.; Yu, M.; Chen, P.; Wang, Y.; Wu, J.; Luo, D.; Tu, Y.; Zhao, L.; Gong, Q.; Zhu, R. Superior Carrier Lifetimes Exceeding 6 Ms in Polycrystalline Halide Perovskites. *Advanced Materials* **2020**, *32* (39), 2002585. https://doi.org/10.1002/adma.202002585.

(31) Kuang, Y.; Zardetto, V.; van Gils, R.; Karwal, S.; Koushik, D.; Verheijen, M. A.; Black, L. E.; Weijtens, C.; Veenstra, S.; Andriessen, R.; Kessels, W. M. M.; Creatore, M. Low-Temperature Plasma-Assisted Atomic-Layer-Deposited SnO2as an Electron Transport Layer in Planar Perovskite Solar Cells. *ACS Appl Mater Interfaces* **2018**, *10* (36), 30367–30378. https://doi.org/10.1021/acsami.8b09515.

(32) Najarian, A. M.; Vafaie, M.; Johnston, A.; Zhu, T.; Wei, M.; Saidaminov, M. I.; Yi, H.; Hoogland, S.; de Arquer, F. P. G.; Sargent, E. H. Sub-Millimetre Light Detection and Ranging Using Perovskites. *Nat Electron* **2022**, *5*, 511–518. https://doi.org/10.1038/s41928-022-00799-7.

(33) Yi, L.; Hou, B.; Zhao, H.; Liu, X. X-Ray-to-Visible Light-Field Detection through Pixelated Colour Conversion. *Nature* **2023**, *618* (7964), 281–286. https://doi.org/10.1038/s41586-023-05978-w.

(34) Deumel, S.; van Breemen, A.; Gelinck, G.; Peeters, B.; Maas, J.; Verbeek, R.; Shanmugam, S.; Akkerman, H.; Meulenkamp, E.; Huerdler, J. E.; Acharya, M.; García-Batlle, M.; Almora, O.;

Guerrero, A.; Garcia-Belmonte, G.; Heiss, W.; Schmidt, O.; Tedde, S. F. High-Sensitivity High-Resolution X-Ray Imaging with Soft-Sintered Metal Halide Perovskites. *Nat Electron* **2021**, *4* (9), 681–688. https://doi.org/10.1038/s41928-021-00644-3.

(35) van Breemen, A. J. J. M.; Ollearo, R.; Shanmugam, S.; Peeters, B.; Peters, L. C. J. M.; van de Ketterij, R. L.; Katsouras, I.; Akkerman, H. B.; Frijters, C. H.; Di Giacomo, F.; Veenstra, S.; Andriessen, R.; Janssen, R. A. J.; Meulenkamp, E. A.; Gelinck, G. H. A Thin and Flexible Scanner for Fingerprints and Documents Based on Metal Halide Perovskites. *Nat Electron* **2021**, *4* (11), 818–826. https://doi.org/10.1038/s41928-021-00662-1.

(36) *Acuros® 6 CQD® SWIR Sensor Preliminary Product Sheet*. https://www.swirvisionsystems.com/wp-content/uploads/2024/01/Acuros6-Sensor-ProductSheet_0124.pdf.

(37) Takase, M.; Miyake, Y.; Yamada, T.; Tamaki, T.; Murakami, M.; Inoue, Y. First Demonstration of 0.9 Mm Pixel Global Shutter Operation by Novel Charge Control in Organic Photoconductive Film. In *2015 International Electron Devices Meeting (IEDM)*; IEEE, 2015; Vol. 2016-February, pp 30.2.1-30.2.4.

(38) Steckel, J. S.; Josse, E.; Pattantyus-Abraham, A. G.; Bidaud, M.; Mortini, B.; Bilgen, H.; Arnaud, O.; Allegret-Maret, S.; Saguin, F.; Mazet, L.; Lhostis, S.; Berger, T.; Haxaire, K.; Chapelon, L. L.; Parmigiani, L.; Gouraud, P.; Brihoum, M.; Bar, P.; Guillermet, M.; Favreau, S.; Duru, R.; Fantuz, J.; Ricq, S.; Ney, D.; Hammad, I.; Roy, D.; Arnaud, A.; Vianne, B.; Nayak, G.; Virollet, N.; Farys, V.; Malinge, P.; Tournier, A.; Lalanne, F.; Crocherie, A.; Galvier, J.; Rabary, S.; Noblanc, O.; Wehbe-Alause, H.; Acharya, S.; Singh, A.; Meitzner, J.; Aher, D.; Yang, H.; Romero, J.; Chen, B.; Hsu, C.; Cheng, K. C.; Chang, Y.; Sarmiento, M.; Grange, C.; Mazaleyrat, E.; Rochereau, K. 1.62 Mm Global Shutter Quantum Dot Image Sensor Optimized for Near and Shortwave Infrared. In *2021 International Electron Devices Meeting (IEDM)*; IEEE, 2021; pp 23.4.1-23.4.4.

(39) Lee, J.; Georgitzikis, E.; Li, Y.; Lin, Z.; Park, J.; Lieberman, I.; Cheyns, D.; Jayapala, M.; Lambrechts, A.; Thijs, S.; Stahl, R.; Malinowski, P. E. Imaging in Short-Wave Infrared with 1.82 Mm Pixel Pitch Quantum Dot Image Sensor. In *2020 International Electron Devices Meeting (IEDM)*; IEEE, 2020; Vol. 2020-December, pp 16.5.1-16.5.4.

(40) Razera, R. A. Z.; Jacobs, D. A.; Fu, F.; Fiala, P.; Dussouillez, M.; Sahli, F.; Yang, T. C. J.; Ding, L.; Walter, A.; Feil, A. F.; Boudinov, H. I.; Nicolay, S.; Ballif, C.; Jeangros, Q. Instability of P-i-n Perovskite Solar Cells under Reverse Bias. *J Mater Chem A Mater* **2020**, *8* (1), 242–250. https://doi.org/10.1039/c9ta12032g.

(41) Ding, H.; Li, B.; Zareen, S.; Li, G.; Tu, Y.; Zhang, D.; Cao, X.; Xu, Q.; Yang, S.; Tait, S. L.; Zhu, J. In Situ Investigations of Al/Perovskite Interfacial Structures. *ACS Appl Mater Interfaces* **2020**, *12* (25), 28861–28868. https://doi.org/10.1021/ACSAMI.0C06458/SUPPL_FILE/AM0C06458_SI_001.PDF.

(42) Lim, J.; Choi, E.; Kim, M.; Lee, M.; Chen, D.; Green, M. A.; Seidel, J.; Kim, C.; Park, J.; Hao, X.; Yun, J. S. Revealing the Dynamics of the Thermal Reaction between Copper and Mixed Halide Perovskite Solar Cells. *ACS Appl Mater Interfaces* **2022**, *14* (18), 20866–20874. https://doi.org/10.1021/ACSAMI.2C01061/SUPPL_FILE/AM2C01061_SI_001.PDF.

(43) Boyd, C. C.; Cheacharoen, R.; Bush, K. A.; Prasanna, R.; Leijtens, T.; McGehee, M. D. Barrier Design to Prevent Metal-Induced Degradation and Improve Thermal Stability in Perovskite Solar Cells. *ACS Energy Lett* **2018**, *3* (7), 1772–1778. https://doi.org/10.1021/acsenergylett.8b00926.

(44) Ni, Z.; Jiao, H.; Fei, C.; Gu, H.; Xu, S.; Yu, Z.; Yang, G.; Deng, Y.; Jiang, Q.; Liu, Y.; Yan, Y.; Huang, J. Evolution of Defects during the Degradation of Metal Halide Perovskite Solar Cells under Reverse Bias and Illumination. *Nat Energy* **2022**, *7* (1), 65–73. https://doi.org/10.1038/s41560-021-00949-9.

(45) Malinowski, P.; Pejovic, V.; Lieberman, I.; Kim, J. H.; Siddik, A. B.; Georgitzikis, E.; Lim, M. J.; Moreno Hagelsieb, L.; Hermans, Y.; Pintor Monroy, I.; Song, W.; Basak, S.; Gehlhaar, R.; De Roose, F.; Siskos, A.; Papadopoulos, N.; Thijs, S.; Verschooten, T.; Chandrasekaran, N.; Li, Y.; SOUSSAN, P.; Genoe, J.; Heremans, P.; Lee, J.; Cheyns, D. Image Sensors Using Thin-Film Absorbers. *Appl Opt* **2023**, *62* (17), 21–30. https://doi.org/10.1364/ao.485552.

(46) Tutundzic, M.; Zhang, X.; Lammar, S.; Singh, S.; Marchezi, P.; Merckx, T.; Aguirre, A.; Moons, E.; Aernouts, T.; Kuang, Y.; Vermang, B. Towards Efficient and Fully Scalable Sputtered NiO_x-based Inverted Perovskite Solar Modules via Coordinated Modification Strategies. *Solar RRL* **2023**, 2300862.

(47) Zhang, X.; Qiu, W.; Apergi, S.; Singh, S.; Marchezi, P.; Song, W.; Sternemann, C.; Elkhouly, K.; Zhang, D.; Aguirre, A.; Merckx, T.; Krishna, A.; Shi, Y.; Bracesco, A.; Van Helvoirt, C.; Bens, F.; Zardetto, V.; Haen, J. D. '; Yu, A.; Brocks, G.; Aernouts, T.; Moons, E.; Tao, S.; Zhan, Y.; Kuang, Y.; Poortmans, J. Minimizing the Interface-Driven Losses in Inverted Perovskite Solar Cells and Modules. https://doi.org/10.1021/acsenergylett.3c00697.

(48) Ollearo, R.; Wang, J.; Dyson, M. J.; Weijtens, C. H. L.; Fattori, M.; van Gorkom, B. T.; van Breemen, A. J. J. M.; Meskers, S. C. J.; Janssen, R. A. J.; Gelinck, G. H. Ultralow Dark Current in Near-Infrared Perovskite Photodiodes by Reducing Charge Injection and Interfacial Charge Generation. *Nat Commun* **2021**, *12* (1), 1–9. https://doi.org/10.1038/s41467-021-27565-1.

(49) Sun, T.; Chen, T.; Chen, J.; Lou, Q.; Liang, Z.; Li, G.; Lin, X.; Yang, G.; Zhou, H. High-Performance p-i-n Perovskite Photodetectors and Image Sensors with Long-Term Operational Stability Enabled by a Corrosion-Resistant Titanium Nitride Back Electrode. *Nanoscale* **2023**, *15* (17), 7803–7811. https://doi.org/10.1039/d3nr00410d.

(50) Lee, W.; Lee, J.; Yun, H.; Kim, J.; Park, J.; Choi, C.; Kim, D. C.; Seo, H.; Lee, H.; Yu, J. W.; Lee, W. B.; Kim, D. H. High-Resolution Spin-on-Patterning of Perovskite Thin Films for a Multiplexed Image Sensor Array. *Advanced Materials* **2017**, *29* (40), 1702902. https://doi.org/10.1002/adma.201702902.

(51) Wu, W.; Wang, X.; Han, X.; Yang, Z.; Gao, G.; Zhang, Y.; Hu, J.; Tan, Y.; Pan, A.; Pan, C. Flexible Photodetector Arrays Based on Patterned CH3NH3PbI3−xClx Perovskite Film for Real-Time Photosensing and Imaging. *Advanced Materials* **2019**, *31* (3). https://doi.org/10.1002/adma.201805913.

(52) Quimby, R. S. *Photonics and Lasers : An Introduction*; Wiley-Interscience, 2006.

(53) Shen, L.; Fang, Y.; Wang, D.; Bai, Y.; Deng, Y.; Wang, M.; Lu, Y.; Huang, J. A Self-Powered, Sub-Nanosecond-Response Solution-Processed Hybrid Perovskite Photodetector for Time-Resolved Photoluminescence-Lifetime Detection. *Advanced Materials* **2016**, *28* (48), 10794–10800. https://doi.org/10.1002/adma.201603573.

(54) Zhang, X.; Eurelings, S.; Bracesco, A.; Song, W.; Lenaers, S.; Van Gompel, W.; Krishna, A.; Aernouts, T.; Lutsen, L.; Vanderzande, D.; Creatore, M.; Zhan, Y.; Kuang, Y.; Poortmans, J. Surface Modulation via Conjugated Bithiophene Ammonium Salt for Efficient Inverted Perovskite Solar Cells. *ACS Appl Mater Interfaces* **2023**, *15*, 46803–46811. https://doi.org/10.1021/acsami.3c08119.

(55) Syed, A. A.; Cai, L.; Zhu, F. High Built-in Potential Perovskite Solar Cells Realized by Incorporating a Hybrid Hole Extraction Layer. *Solar RRL* **2020**, *4* (11), 2000393. https://doi.org/10.1002/solr.202000393.

(56) Li, X.; Zhang, W.; Guo, X.; Lu, C.; Wei, J.; Fang, J. Constructing Heterojunctions by Surface Sulfidation for Efficient Inverted Perovskite Solar Cells. *Science (1979)* **2022**, *375*, 434–437.

(57) *EMVA Standard 1288 Standard for Characterization of Image Sensors and Cameras*; 2021. www.emva.org.

(58) Machida, S.; Shishido, S.; Tokuhara, T.; Yanagida, M.; Yamada, T.; Izuchi, M.; Sato, Y.; Miyake, Y.; Nakata, M.; Murakami, M.; Harada, M.; Inoue, Y. A 2.1Mpixel Organic-Film Stacked RGB-IR Image Sensor with Electrically Controllable IR Sensitivity. In *Digest of Technical Papers - IEEE International Solid-State Circuits Conference*; Institute of Electrical and Electronics Engineers Inc., 2017; Vol. 60, pp 78–79. https://doi.org/10.1109/ISSCC.2017.7870269.

(59) Nishimura, K.; Sato, Y.; Hirase, J.; Sakaida, R.; Yanagida, M.; Tamaki, T.; Takase, M.; Kanehara, H.; Murakami, M.; Inoue, Y. An over 120dB Simultaneous-Capture Wide-Dynamic-Range 1.6e- Ultra-Low-Reset-Noise Organic-Photoconductive-Film CMOS Image Sensor. In *Digest of Technical Papers - IEEE International Solid-State Circuits Conference*; Institute of Electrical and Electronics Engineers Inc., 2016; Vol. 59, pp 110–111. https://doi.org/10.1109/ISSCC.2016.7417931.

(60) Kang, J.; Park, Y.; Hwang, J. H.; Hong, K.; Son, I.; Chun, J. H.; Choi, J.; Kim, S. J. An Indirect Time-of-Flight Sensor with Tetra-Pixel Architecture Calibrating Tap Mismatch in a Single Frame. *IEEE Solid State Circuits Lett* **2022**, *5*, 284–287. https://doi.org/10.1109/LSSC.2022.3225722.

(61) Keel, M. S.; Jin, Y. G.; Kim, Y.; Kim, D.; Kim, Y.; Bae, M.; Chung, B.; Son, S.; Kim, H.; An, T.; Choi, S. H.; Jung, T.; Kwon, Y.; Seo, S.; Kim, S. Y.; Bae, K.; Shin, S. C.; Ki, M.; Yoo, S.; Moon, C. R.; Ryu, H.; Kim, J. A VGA Indirect Time-of-Flight CMOS Image Sensor with 4-Tap 7-Mm Global-Shutter Pixel and Fixed-Pattern Phase Noise Self-Compensation. *IEEE J Solid-State Circuits* **2020**, *55* (4), 889–897. https://doi.org/10.1109/JSSC.2019.2959502.

(62) Kang, J.; Park, Y.; Hwang, J. H.; Chun, J. H.; Choi, J.; Kim, S. J. A 640×480 Indirect Time-of-Flight Image Sensor with Tetra Pixel Architecture for Tap Mismatch Calibration and Motion Artifact Suppression. In *2022 Symposium on VLSI Technology*; IEEE, 2022; Vol. 2022-June, pp 44–45. https://doi.org/10.1109/VLSITECHNOLOGYANDCIR46769.2022.9830477.

(63) Park, J.; Kim, D.; Lee, H.; Shin, S. C.; Ki, M.; Chung, B.; Bae, M.; Kye, M.; Ahn, J.; Song, I.; Lee, S.; An, J.; Hwang, I. P.; An, T.; Jin, Y. G.; Kim, Y.; Oh, Y.; Ko, J.; Lee, H.; Yim, J. S. An Indirect Time-of-Flight CMOS Image Sensor Achieving Sub-Ms Motion Lagging and 60fps Depth Image from On-Chip ISP. In *2023 Symposium on VLSI Technology*; IEEE, 2023; Vol. 2023-June, pp 1–2. https://doi.org/10.23919/VLSITECHNOLOGYANDCIR57934.2023.10185418.

(64) Fan, Y.; Wang, Y.; Zhang, N.; Sun, W.; Gao, Y.; Qiu, C. W.; Song, Q.; Xiao, S. Resonance-Enhanced Three-Photon Luminesce via Lead Halide Perovskite Metasurfaces for Optical Encoding. *Nat Commun* **2019**, *10* (1). https://doi.org/10.1038/s41467-019-10090-7.

(65) Zhizhchenko, A. Y.; Cherepakhin, A. B.; Masharin, M. A.; Pushkarev, A. P.; Kulinich, S. A.; Porfirev, A. P.; Kuchmizhak, A. A.; Makarov, S. V. Direct Imprinting of Laser Field on Halide Perovskite Single Crystal for Advanced Photonic Applications. *Laser Photon Rev* **2021**, *15* (8). https://doi.org/10.1002/lpor.202100094.

(66) Kim, D.; Lee, S.; Park, D.; Piao, C.; Park, J.; Ahn, Y.; Cho, K.; Shin, J.; Song, S. M.; Kim, S. J.; Chun, J. H.; Choi, J. Indirect Time-of-Flight CMOS Image Sensor with On-Chip Background Light Cancelling and Pseudo-Four-Tap/Two-Tap Hybrid Imaging for Motion Artifact Suppression. *IEEE J Solid-State Circuits* **2020**, *55* (11), 2849–2865. https://doi.org/10.1109/JSSC.2020.3021246.

(67) Okada, C.; Yokogawa, S.; Yorikado, Y.; Honda, K.; Okuno, N.; Ikeno, R.; Yamakoshi, M.; Ito, H.; Yoshitsune, S.; Desaki, M.; Hida, S.; Nose, A.; Wakabayashi, H.; Koga, F. 216 Fps 672 × 512 Pixel 3 Mm Indirect Time-of-Flight Image Sensor with 1-Frame Depth Acquisition for Motion Artifact Suppression. In *2023 Symposium on VLSI Technology*; IEEE, 2023; Vol. 2023-June, pp 1–2.

(68) Piao, C.; Ahn, Y.; Kim, D.; Park, J.; Kang, J.; Shin, M.; Seo, K.; Kim, S. J.; Chun, J. H.; Choi, J. A 70mW Indirect Time-of-Flight Image Sensor with Depth Dynamic Range Enhancement and Fixed Depth Noise Compensation. In *2021 Asian Solid-State Circuits Conference (ASSCC)*; IEEE, 2021; pp 13.6.1-13.6.3.

(69) Xue, J.; Zhu, Z.; Xu, X.; Gu, Y.; Wang, S.; Xu, L.; Zou, Y.; Song, J.; Zeng, H.; Chen, Q. Narrowband Perovskite Photodetector-Based Image Array for Potential Application in Artificial Vision. *Nano Lett* **2018**, *18* (12), 7628–7634. https://doi.org/10.1021/acs.nanolett.8b03209.

(70) Zhu, H. L.; Lin, H.; Song, Z.; Wang, Z.; Ye, F.; Zhang, H.; Yin, W. J.; Yan, Y.; Choy, W. C. H. Achieving High-Quality Sn-Pb Perovskite Films on Complementary Metal-Oxide-Semiconductor-Compatible Metal/Silicon Substrates for Efficient Imaging Array. *ACS Nano* **2019**, *13* (10), 11800–11808. https://doi.org/10.1021/acsnano.9b05774.

(71) Hou, Y.; Li, J.; Yoon, J.; Knoepfel, A. M.; Yang, D.; Zheng, L.; Ye, T.; Ghosh, S.; Priya, S.; Wang, K. Retina-Inspired Narrowband Perovskite Sensor Array for Panchromatic Imaging. *Sci Adv* **2023**, *9* (15), eade2338. https://doi.org/10.1126/SCIADV.ADE2338/SUPPL_FILE/SCIADV.ADE2338_SM.PDF.

(72) Liu, Y.; Ji, Z.; Cen, G.; Sun, H.; Wang, H.; Zhao, C.; Wang, Z. L.; Mai, W. Perovskite-Based Color Camera Inspired by Human Visual Cells. *Light Sci Appl* **2023**, *12* (1), 43. https://doi.org/10.1038/s41377-023-01072-y.

(73) Tang, Y.; Jin, P.; Wang, Y.; Li, D.; Chen, Y.; Ran, P.; Fan, W.; Liang, K.; Ren, H.; Xu, X.; Wang, R.; Yang, Y. (Michael); Zhu, B. Enabling Low-Drift Flexible Perovskite Photodetectors by Electrical Modulation for Wearable Health Monitoring and Weak Light Imaging. *Nat Commun* **2023**, *14*, 4961. https://doi.org/10.1038/s41467-023-40711-1.

(74) Wang, T.; Zheng, D.; Vegso, K.; Mrkyvkova, N.; Siffalovic, P.; Pauporté, T. High-Resolution and Stable Ruddlesden–Popper Quasi-2D Perovskite Flexible Photodetectors Arrays for Potential Applications as Optical Image Sensor. *Adv Funct Mater* **2023**, *33* (43), 2304659. https://doi.org/10.1002/ADFM.202304659.